Progress In Electromagnetics Research C, Vol. 171, 492–500, 2026
PIER C
(Received 19 April 2026, Accepted 9 July 2026, Scheduled 16 July 2026)

# Simulation Research on Electromagnetic Interference for Motor Drive System of Electric Vehicle

Tianhong Tan[1,*], Tao Jiang[1], and Hui Ke[2]

[1]College of Information and Communication Engineering, Harbin Engineering University, Harbin, Heilongjiang, China
[2]Changchun Technical University of Automobile, Changchun, Jilin, China

**ABSTRACT:** An electric drive system is a core component of electric vehicles, and its electromagnetic compatibility (EMC) is critical to vehicle safety. Addressing the difficulty of locating electromagnetic interference (EMI) coupling paths via testing alone, this paper presents a simulation study of conducted EMI in motor drive systems. Parasitic parameters of key components are extracted through impedance testing and 3D electromagnetic simulation. Based on transmission line theory and impedance fitting, high-frequency equivalent models of each unit are developed and integrated into a system-level EMI simulation model. Validation shows that the model predicts conducted interference below 30 MHz accurately, with errors within 6 dB below 1 MHz and less than 10 dB in the 1 MHz–30 MHz band. This model enables rapid EMC troubleshooting and provides reliable simulation support for the forward design of electric vehicle drive systems.

## 1. INTRODUCTION

This paper focuses on high-voltage (HV) components, which are typical electromagnetic emission sources in electric drive systems and are the main cause of electromagnetic compatibility (EMC) problems on the low-voltage (LV) side. The electrical structure of the drive system is illustrated in Fig. 1. In the HV circuit, the power battery supplies high-voltage DC power to the motor drive system through HV DC buses and connectors. The DC power is then converted into three-phase AC power by a three-phase full-bridge inverter composed of six insulated-gate bipolar transistors (IGBTs) to drive the permanent magnet synchronous motor [1].

Relevant research has been widely conducted. Pareschi et al. analyzed mainstream technologies of spread-spectrum clock generators and theoretically verified that specific triangular driving frequencies can maximally suppress spectral peaks, while no simulation or experimental verification was performed [2]. Zare proposed a high-frequency motor modeling method to predict leakage current and shaft voltage. However, the adopted model was overly simplified without considering stray capacitances, leading to discrepancies between simulation and measurement results [3]. Jia et al. investigated common-mode and differential-mode interference paths of vehicle drive systems and established Simulation Program with Integrated Circuit Emphasis (SPICE) and Simulink models for key components. Nevertheless, their method fails to accurately predict conducted interference below 30 MHz [4].

To address the above limitations, this paper establishes a complete electromagnetic simulation model for electric drive systems. The EMI coupling paths and effects of parasitic parameters, loop areas, and other key factors are analyzed. This work integrates EMC design into the early development stage to select optimal schemes and realize the forward EMC design in electric drive systems.

* Corresponding author: Tianhong Tan (tthjob@163.com).

## 2. ANALYSIS OF ELECTROMAGNETIC INTERFERENCE IN MOTOR DRIVE SYSTEM

Conducted interference is a typical electromagnetic interference problem in a motor drive system, which can be divided into two parts: common mode interference and differential mode interference, shown in Figure 2 and Figure 3.

Differential mode interference is caused by parasitic inductance, which makes the interference signal form a loop between the positive and negative poles of the power supply.

Therefore, the main characteristic of differential-mode interference is that the currents in the two conductors of the loop are equal in magnitude but opposite in direction relative to each other — one conductor carries the forward current while the other carries the return current. The capacitance is in a low-impedance state at high frequency, and the inductance is in a low-impedance state at low frequency. Therefore, the common-mode interference is mainly reflected in the relatively high frequency, while the differential-mode interference is to the contrary. The frequency limit is usually about 1 MHz. The whole conducted interference is most easily reflected below 30 MHz [5, 6].

## 3. SIMULATION MODELING OF ELECTRIC DRIVE SYSTEM

The simulation models for different components, such as motor controller, cable, motor, and Line Impedance Stabilization Network, are constructed, respectively. The common-mode impedance and differential-mode impedance are measured by a

doi:10.2528/PIERC26041901

Published by THE ELECTROMAGNETIC ACADEMY

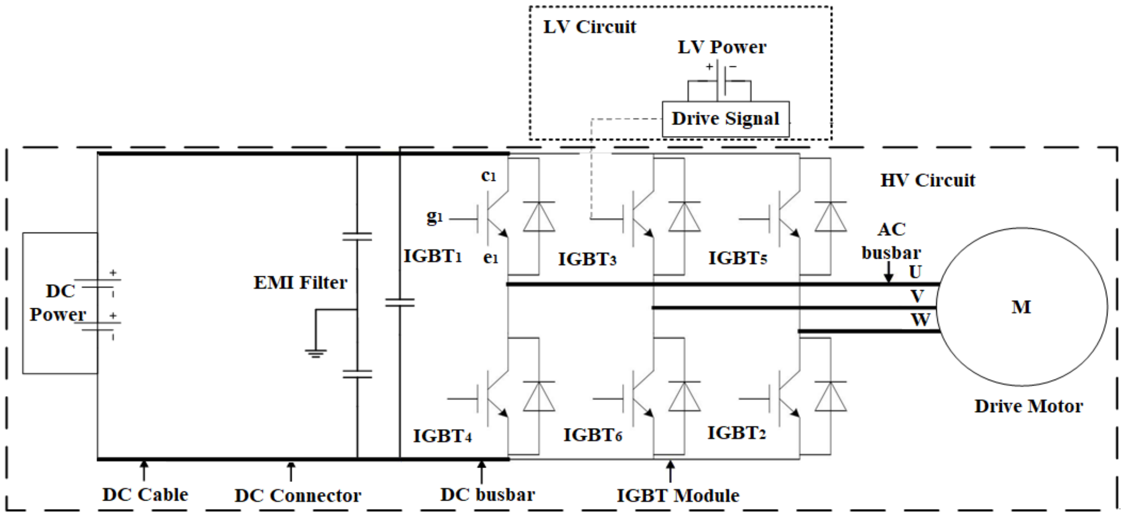


FIGURE 1. Electrical structure of motor drive system.

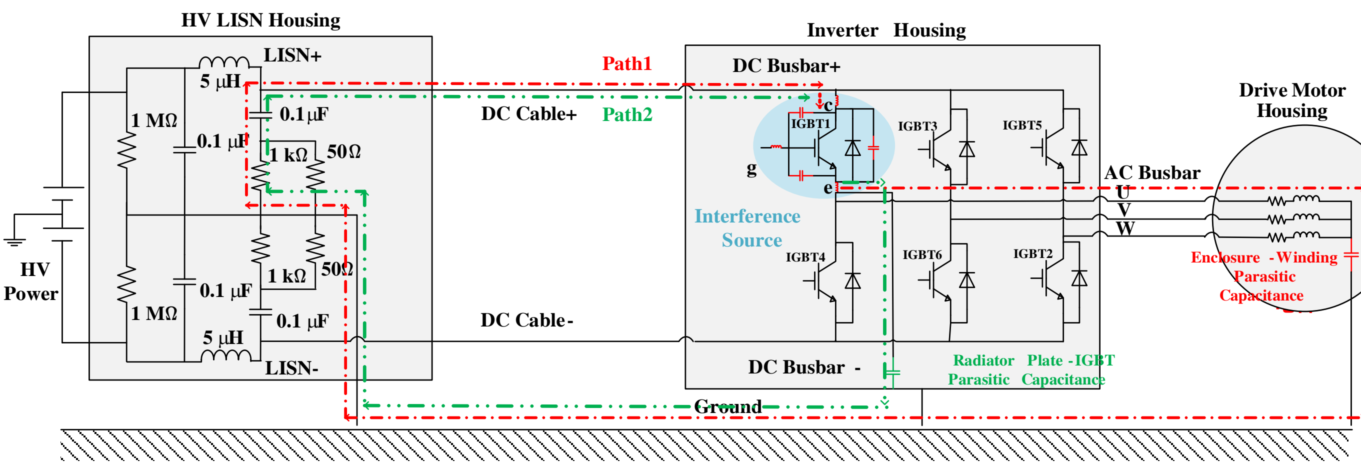


FIGURE 2. Path of common-mode interference.

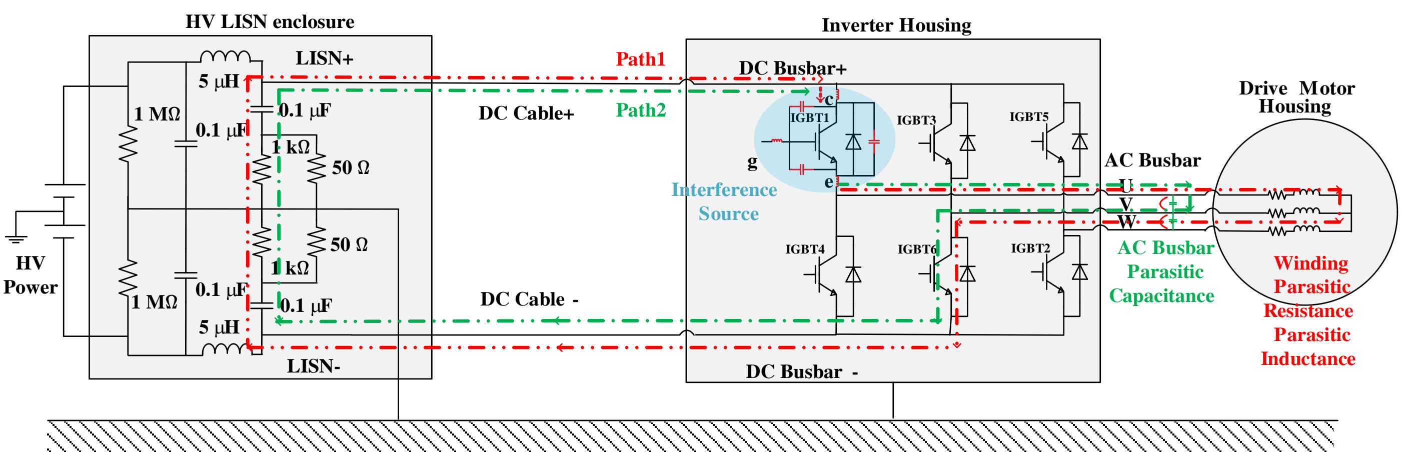


FIGURE 3. Path of differential-mode interference.

vector network analyzer. Then, according to the physical structure of each component, the high-frequency equivalent circuit model is established, and the common-mode and differential-mode impedances are calculated. According to the resonance point value of the measured impedance, the inductance, capacitance, and resistance values of the high-frequency equivalent circuit components are calculated, so that the calculated impedance is consistent with the measured impedance in the full frequency band, and the common-mode and differential-mode effects of each component are covered by the model. The model to be built mainly includes a high-voltage connection system, an IGBT module, and a motor. As an example, the method of motor modeling is described in this paper.

### 3.1. LISN Model

Line Impedance Stabilization Network (LISN), shown in Figure 4 and also known as an artificial mains network, is an essential device for conducted electromagnetic interference (EMI) testing of electric vehicle drive systems. Designed in accordance with the CISPR 25 automotive EMC standard, it mainly isolates grid noise, provides standardized and stable impedance, and extracts high-frequency interference signals from the equipment under test, so as to ensure consistent and accurate test results. It suppresses noise from the power-supply side, offers standard test impedance, and also functions as a filter in the test system.

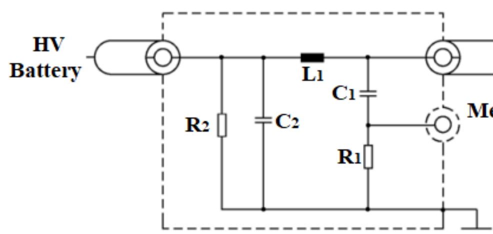


**FIGURE 4**. LISN model.

The LISN is equipped with three ports. The first port is connected to a high-voltage traction battery; the second port is linked to the high-voltage wiring of the equipment under test; the third port serves as the measurement port and is connected to an EMI test receiver via a coaxial cable. In this simulation, the LISN model is built with simulation software, following the CISPR 25 standard. The detailed parameters are presented as follows:

$L_1 = 5\,\mu\text{H}$, $R_1 = 1\,\text{kohm}$, $C_1 = 0.1\,\mu\text{F}$, $C_2 = 0.1\,\mu\text{F}$.

### 3.2. High-Voltage Connection System

According to high-frequency circuit theory, when conductors, such as cables and busbars, operate under high-frequency conditions, the wavelength of the current approaches the geometric length of the conductors [7–11]. The impacts of parasitic parameters, including the inherent resistance and inductance of conductors, as well as the distributed capacitance and conductance between lines, are significantly intensified. The phase shift during signal transmission becomes increasingly prominent, and the traditional lumped-parameter circuit model can no longer accurately characterize their electrical properties. Therefore, this paper adopts the distributed-parameter transmission line model for modeling and analysis.

A small segment of the cable is selected for analysis. The high-voltage connecting components are divided into multiple infinitesimal transmission-line units, each consisting of distributed resistance Rdz, inductance Ldz, conductance Gdz, and capacitance Cdz [12–15]. The corresponding topology is shown in Fig. 5. Based on Kirchhoff's laws, the partial differential equations of transmission lines are derived to describe the relationship among voltage, current, and distributed parameters at any position along the line, which serves as the theoretical foundation for the overall modeling.

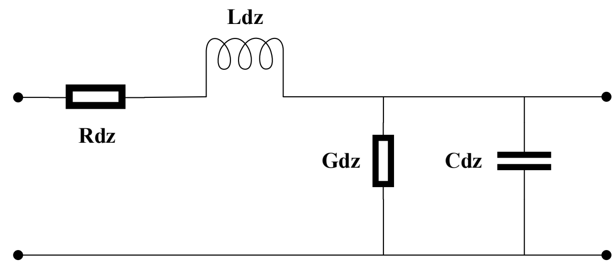


**FIGURE 5**. Microelement transmission line.

According to the above transmission line theory and the actual physical structure and layout of each component, the equivalent circuit topologies of high-voltage DC cables, high-voltage connectors, high-voltage DC busbars, and three-phase AC busbars are established successively, as illustrated in Fig. 6 to Fig. 9. During modeling, structural differences, wiring spacing, and shielding configurations of various components are taken into account fully. The parasitic coupling characteristics, including internal impedance, inter-wire capacitance, and mutual inductance, are accurately reproduced, which completely reflects the propagation and coupling behaviors of high-frequency signals in the high-voltage connection system and lays a solid circuit foundation for subsequent system-level high-frequency electromagnetic simulation.

$$\begin{cases} \dfrac{\partial v\left(z,t\right)}{\partial z} = -Ri\left(z,t\right) - L\dfrac{\partial i\left(z,t\right)}{\partial t} \\ \dfrac{\partial i(z,t)}{\partial z} = -Gv(z,t) - C\dfrac{\partial v(z,t)}{\partial t} \end{cases} \tag{1}$$

This paper uses ANSYS Q3D Extractor to extract the parasitic parameters of all components. During modeling, reasonable geometric simplification is performed on non-critical chamfers of conductors and tiny assembly gaps, while retaining core structures, such as conductor bodies, shielding layers, and electrodes. Mesh refinement is applied to conductor contact surfaces and inter-electrode coupling areas, and adaptive meshing is adopted for other regions. The solving frequency band is set from 15 kHz to 30 MHz. Physical parameters, including electrical conductivity and relative permeability, are assigned according to the actual material parameters of the devices. Finally, full parasitic parameters per unit length, such as resistance, inductance, mutual inductance, and distributed capacitance, are extracted, and the extraction results are presented in Tables 1 to 4.

In addition, to verify the accuracy of the equivalent circuit, a vector network analyzer is used to measure the amplitude-frequency and phase-frequency characteristics of the port impedance of each component. The vector fitting method is adopted to fit the measured impedance curves. By properly selecting the fitting order and setting the convergence threshold,

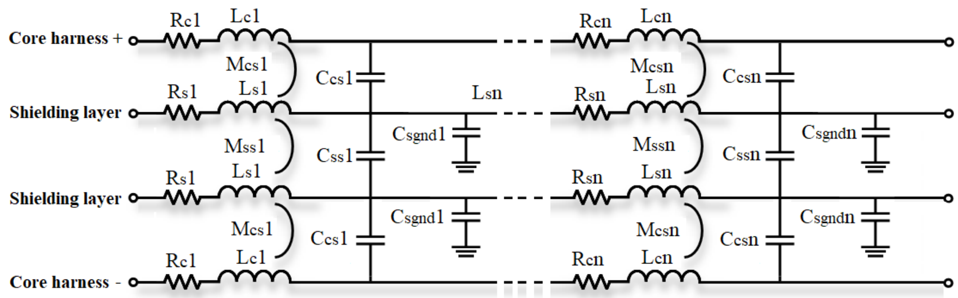


FIGURE 6. High-voltage DC cable.

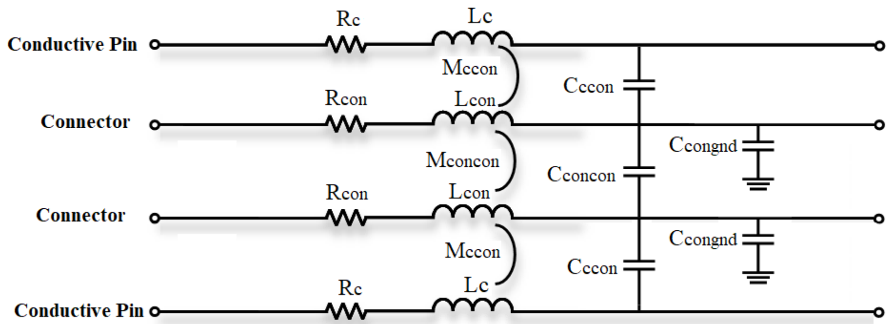


FIGURE 7. High-voltage DC connector.

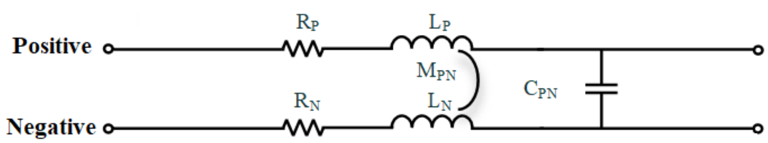


FIGURE 8. High-voltage DC busbar.

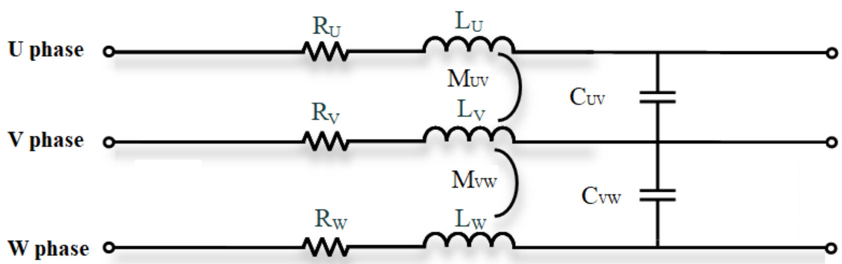


FIGURE 9. High-voltage AC busbar.

the measured impedance is converted into the parameters of the equivalent RLC network. This ensures that the simulated impedance is highly consistent with the measured impedance across the entire frequency band and enables the equivalent model to accurately reproduce high-frequency impedance characteristics of the components.

### 3.3. IGBT Power Module

According to lumped-parameter circuit theory, within a specific frequency band, the high-frequency impedance characteristics of each port of the IGBT can be equivalently represented by an RLC series circuit. In other words, each port can be equivalent to an RLC series circuit, and its topological structure is shown in Fig. 10.

The parasitic parameters in IGBT packaging are one of the main paths of electromagnetic interference, mainly including the inductance and resistance of the pins themselves, as well as the parasitic capacitance between the pins and the heat dissipation board [16, 17]. As shown in Fig. 11, taking a single bridge arm as an example, the parasitic parameters between the IGBT poles and the heat dissipation board are shown in Table 5.

The parasitic parameter circuit between collector c1 and the ground terminal of the heat sink adopts an RLC series

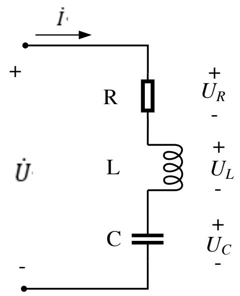


**FIGURE 10.** RLC series circuit.

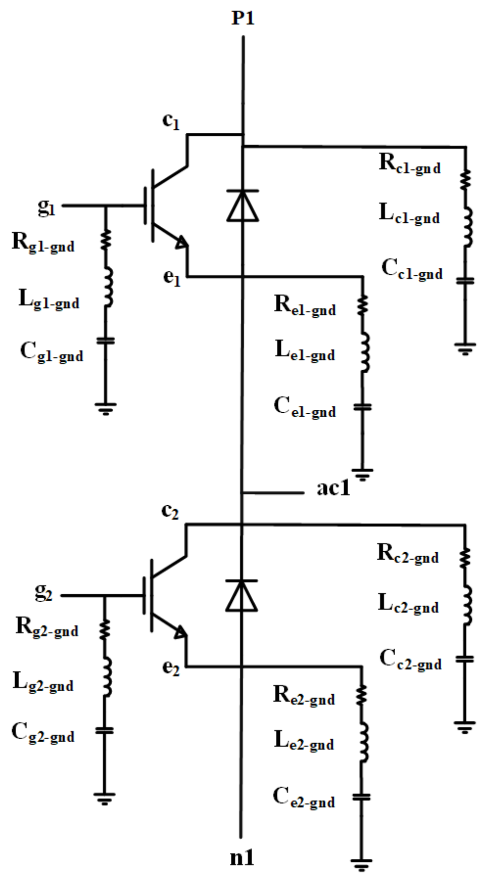


**FIGURE 11.** Model of IGBT.

**TABLE 1.** Parasitic parameters of DC cable.

| Port Name | Parameter | Value |
|---|---|---|
| Core harness | Rc1 | 231.063 μΩ |
| | Lc1 | 385.232 nH |
| Core harness — Shielding layer | Ccs1 | 239.451 pF |
| | Mcs1 | 338.121 nH |
| Shielding layer | Rs1 | 447.746 μΩ |
| | Ls1 | 336.138 nH |
| | Csgnd1 | 359.135 pF |
| Shielding layer — Shielding layer | Css1 | 24.789 pF |
| | Mss1 | 259.383 nH |

**TABLE 2.** Parasitic parameters of DC connector.

| Port Name | Parameter | Value |
|---|---|---|
| Conductive Pin | Rc | 23.1 μΩ |
| | Lc | 20.5 nH |
| Conductive Pin — Connector Housing | Cccon | 0.4 pF |
| | Mccon | 4.1 nH |
| Connector Housing | Rcon | 17.4 μΩ |
| | Lcon | 13.1 nH |
| | Ccongnd | 0.5 pF |
| Connector Housing — Connector Housing | Cconcon | 20.1 pF |
| | Mconcon | 14.1 nH |

**TABLE 3.** Parasitic parameters of DC bus.

| Port Name | Parameter | Value |
|---|---|---|
| Positive | Rp | 81.9 μΩ |
| | Lp | 63.1 nH |
| Positive — Negative | CPN | 58.3 pF |
| | MPN | 41.1 nH |
| Negative | RN | 95.1 μΩ |
| | LN | 75.1 nH |

**TABLE 4.** Parasitic parameters of AC busbar.

| Port Name | Parameter | Value |
|---|---|---|
| U phase | RU | 38.017 μΩ |
| | LU | 38.637 nH |
| U phase — V phase | CUV | 1.585 pF |
| | MUV | 13.352 nH |
| V phase | RV | 36.926 μΩ |
| | LV | 36.460 nH |
| V phase — W phase | CVW | 1.584 pF |
| | MVW | 13.351 nH |
| W phase | RW | 38.017 μΩ |
| | LW | 38.637 nH |

topology, and its impedance characteristic curves are presented in Fig. 12. This figure shows the measured high-frequency impedance curves of the tested component, with the upper plot depicting amplitude-frequency characteristics and the lower plot showing phase-frequency characteristics. At frequencies below 10 MHz, the impedance decreases linearly with increasing frequency, and the phase remains at −90°, indicating a purely capacitive behavior. A distinct series resonance occurs at approximately 20 MHz, where the impedance reaches its minimum value, and the phase changes abruptly. Above 20 MHz, the impedance rises gradually as frequency increases, and the phase approaches 90°, showing inductive characteristics. The curves clearly reveal the dominant effects of parasitic capacitance and inductance across different frequency bands, providing measured data for subsequent equivalent circuit modeling and parameter fitting.

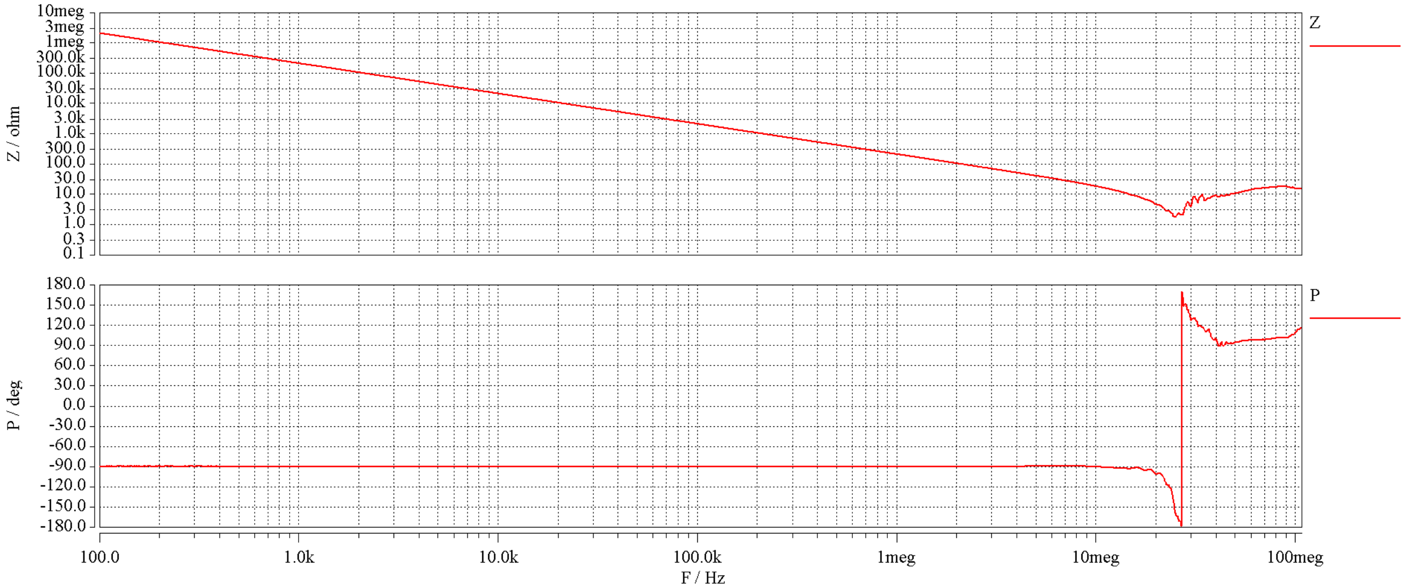


**FIGURE 12**. Impedance test curve of c1-gnd port.

**TABLE 5**. Parasitic parameters between each electrode of IGBT and heat sink.

| Port Name | Parameter | Value |
|---|---|---|
| | Rc1-gnd | 1.711 Ω |
| c1-gnd | Lc1-gnd | 52.456 nH |
| | Cc1-gnd | 767.032 pF |
| | Re1-gnd | 1.498 Ω |
| e1-gnd | Le1-gnd | 60.172 nH |
| | Ce1-gnd | 768.798 pF |
| | Rg1-gnd | 0.303 Ω |
| g1-gnd | Lg1-gnd | 67.075 nH |
| | Cg1-gnd | 765.056 pF |
| | Rc2-gnd | 2.037 Ω |
| c2-gnd | Lc2-gnd | 66.797 nH |
| | Cc2-gnd | 769.444 pF |
| | Re2-gnd | 2.450 Ω |
| e2-gnd | Le2-gnd | 53.865 nH |
| | Ce2-gnd | 758.458 pF |
| | Rg2-gnd | 1.030 Ω |
| g2-gnd | Lg2-gnd | 60.835 nH |
| | Cg2-gnd | 773.335 pF |

### 3.4. Motor Modeling

The EMI model of a permanent magnet synchronous motor is completed by building a "black box" equivalent circuit [18–23]. The impedance characteristic curve of the motor port is obtained through the impedance analyzer test, and the impedance curve is fitted into an RLC network by the vector matching method. The overall model of the motor is shown in Fig. 13. $Z_{dm}$ and $Z_{cm}$ represent single-phase differential mode impedance and single-phase common mode impedance of the motor, respectively.

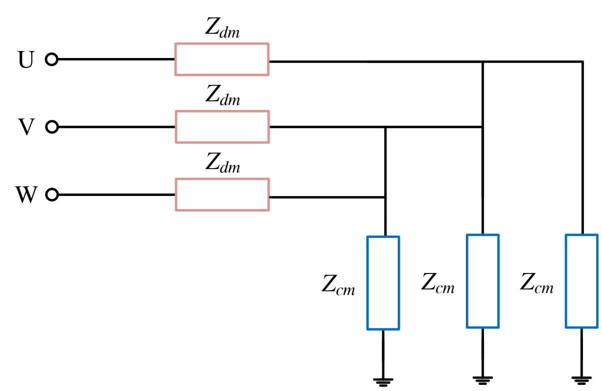


**FIGURE 13**. Typical motor structure model.

$$Z_{CM} = \frac{Z_{dm}}{3} + 3Z_{cm} \tag{2}$$

$$Z_{DM} = \frac{3Z_{dm}}{2} \tag{3}$$

$$Z_{cm} = Z_{CM} - \frac{2Z_{DM}}{3} \tag{4}$$

$$Z_{dm} = \frac{2Z_{DM}}{3} \tag{5}$$

According to the motor common mode impedance test port, three-phase common mode impedance and single-phase common mode impedance are shown in Eq. (1), three-phase differential mode impedance and single differential mode impedance are shown in Eq. (3), where $Z_{CM}$ and $Z_{DM}$ represent three-phase common mode impedance and three-phase differential mode impedance of the motor, respectively. Simplify Eqs. (2) and (3) to obtain the calculation equations of single-phase common mode impedance and single-phase difference mode

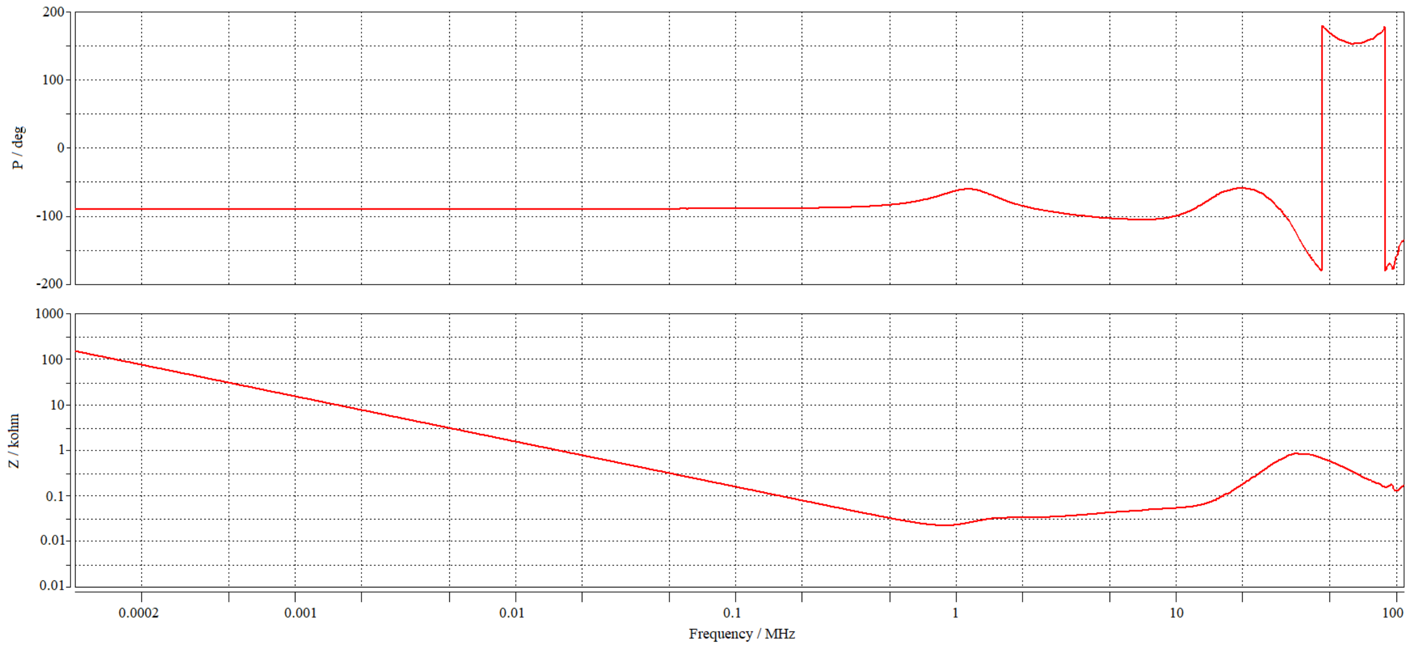


**FIGURE 14**. Single-phase common mode impedance of the motor.

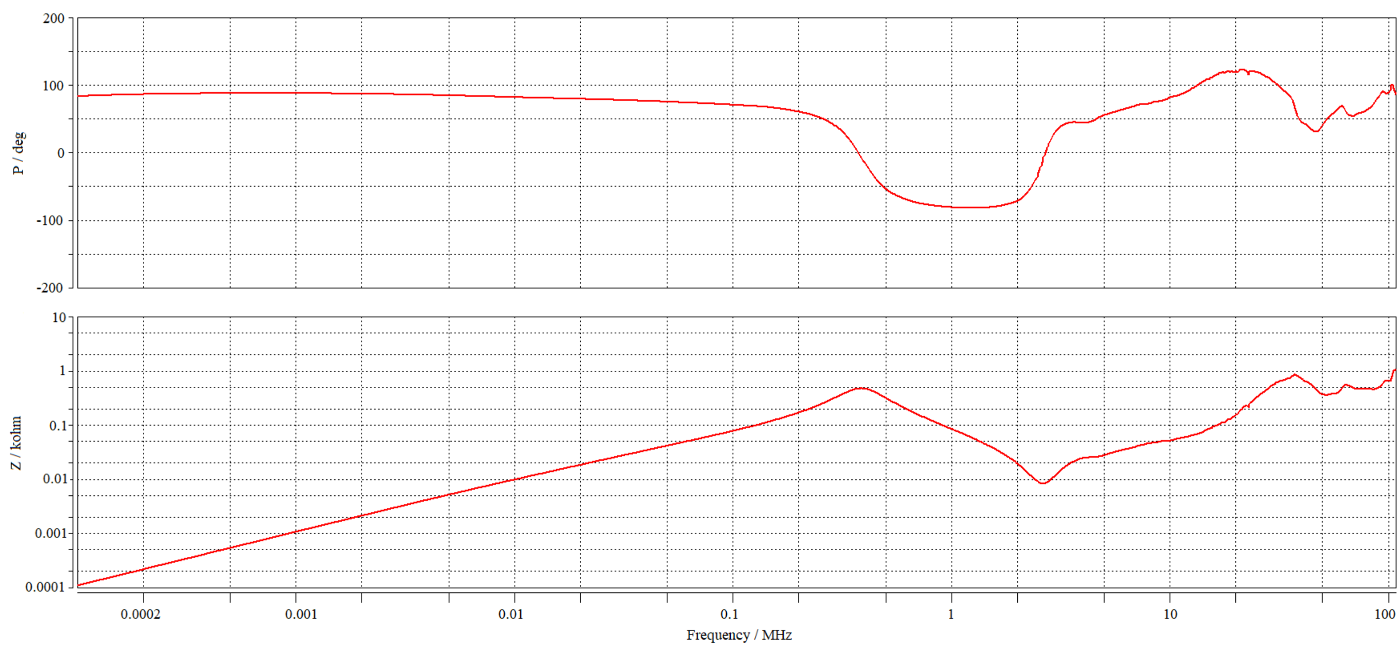


**FIGURE 15**. Single-phase differential mode impedance of the motor.

impedance, as shown in Eqs. (4) and (5). Solve the single-phase common mode impedance and single-phase difference mode impedance of the motor, as shown in Figs. 14 and 15.

## 4. SYSTEM-LEVEL EMI SIMULATION VERIFICATION

Based on the built simulation model, connect the sub-component models to obtain the system-level conducted emission simulation model, as shown in Fig. 16.

The results obtained by comparing the conducted emission simulation results of the motor drive system based on Fig. 16 with the actual test results are shown in Fig. 17.

Figure 17 compares the simulated and measured conducted electromagnetic interference (EMI) of the electric drive system over the frequency range of 9 kHz to 30 MHz, where the blue curve represents the simulation results, and the red curve denotes the test data. Within the standard EMI test band of 150 kHz–30 MHz, the simulated and measured curves show good overall agreement in both trend and key resonance

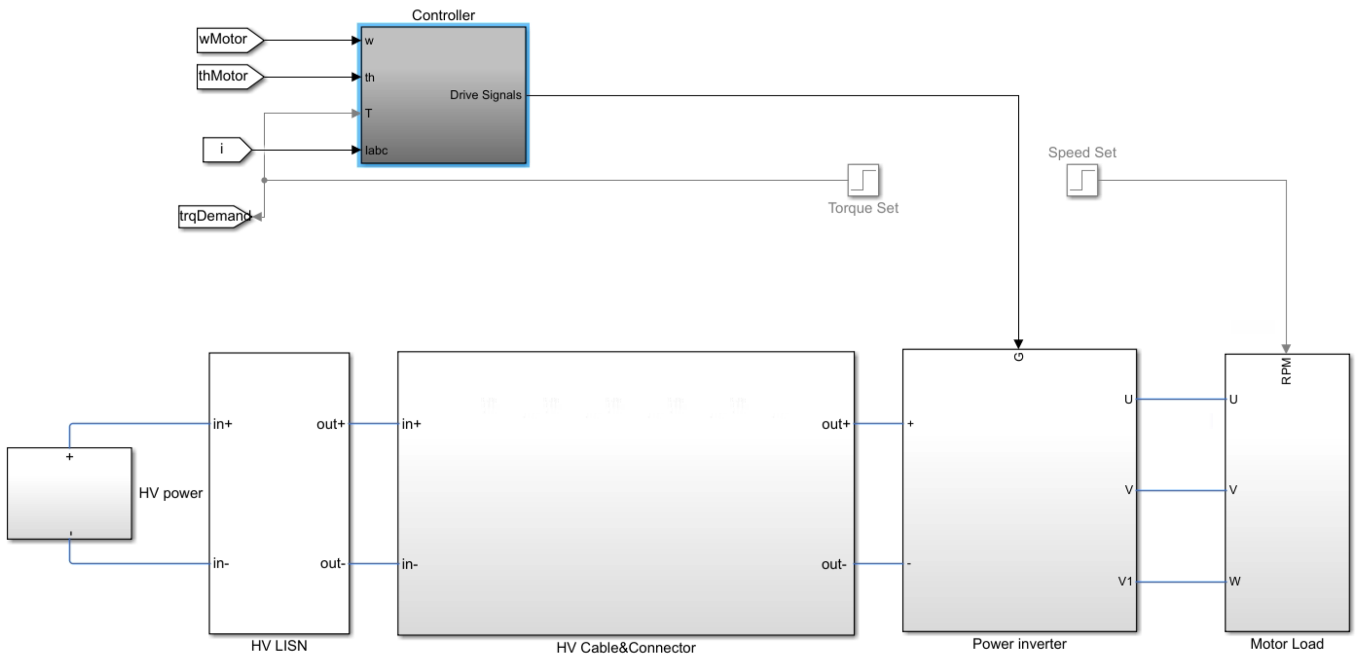


**FIGURE 16**. System-level conducted emission model.

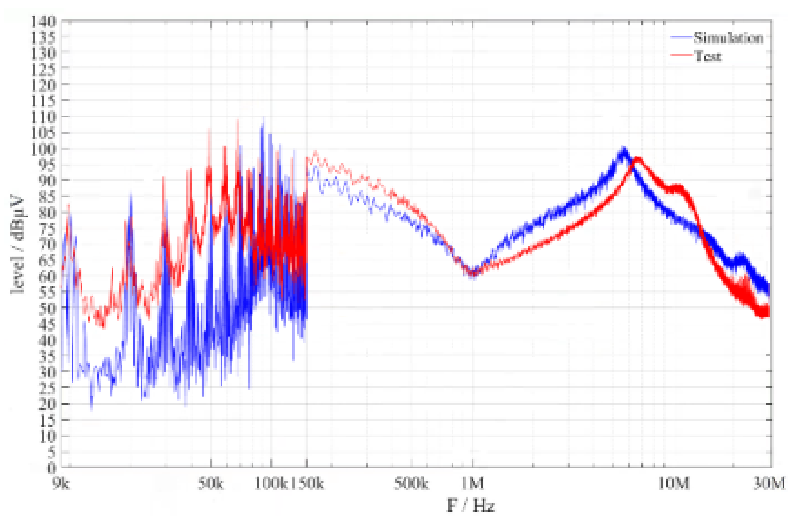


**FIGURE 17**. Comparison of simulation and test results.

peaks, indicating that the proposed system-level electromagnetic model accurately reproduces the main characteristics of conducted interference. In the low-frequency range (9 kHz–150 kHz), some deviations in the amplitudes of switching harmonic spikes are observed, which are mainly attributed to the simplified modeling of the IGBT switching transient process and do not affect the model's prediction accuracy within the standard test band.

As shown in Fig. 17, the simulation agrees well with the test results below 1 MHz, with resonance point errors no greater than 6 dB, demonstrating high model accuracy. In the 1 MHz–30 MHz range, the simulation follows the measured trend closely, with an overall error below 10 dB. In summary, the discrepancies between simulation and measurement are within acceptable limits, verifying the validity and reliability of the model. The proposed model provides solid support for the analysis and optimization of EMC issues in electric drive systems.

## 5. CONCLUSION

This study addresses the conducted electromagnetic interference (EMI) problem in electric vehicle motor drive systems by developing a system-level high-frequency simulation model based on transmission line theory. Parasitic parameters of key components, including high-voltage cables, connectors, IGBT modules, and motors, are extracted to build equivalent circuit models for each unit, which are then integrated into a system model. Experimental validation shows that the resonance point error is no more than 6 dB below 1 MHz, and the overall prediction error is less than 10 dB in the 1 MHz–30 MHz band. The simulated and measured results follow consistent trends, enabling the effective prediction of conducted interference below 30 MHz.

The proposed model provides reliable support for the forward design and optimization of electromagnetic compatibility (EMC) in electric drive systems. In the future, statistical verification will enhance simulation reliability. Uncertainty quantification and sensitivity analysis will also be used to study stray parameters and key coupling paths.

## ACKNOWLEDGEMENT

This study was funded by the National Key Research and Development Program of China (2022YFE0123600), Harbin Engineering University high-level scientific research guidance special "urgent solution" research plan (3072022 QBZ0804), and the Key Laboratory of Advanced Marine Communication and Information Technology, Ministry of Industry and Information Technology, Harbin Engineering University, Harbin, China.

## REFERENCES

[1] Yang, M. and W. Yu, "Efficient generation of 3-D capacitance macromodel based on finite difference method," in *2017 International Applied Computational Electromagnetics Society Symposium (ACES)*, 1–2, Suzhou, China, 2017.

[2] Pareschi, F., G. Setti, R. Rovatti, and G. Frattini, "Practical optimization of EMI reduction in spread spectrum clock generators with application to switching DC/DC converters," *IEEE Transactions on Power Electronics*, Vol. 29, No. 9, 4646–4657, 2014.

[3] Zare, F., "Practical approach to model electric motors for electromagnetic interference and shaft voltage analysis," *IET Electric Power Applications*, Vol. 4, No. 9, 727–738, 2010.

[4] Jia, J., X. Hu, Y. Xia, Q. Chen, X. Wu, and Y. Long, "Research on modelling method of conducted EMI in the electric drive system on motor-load conditions," in *2024 International Symposium on Electromagnetic Compatibility — EMC Europe*, 804–809, Brugge, Belgium, 2024.

[5] Tan, T. and T. Jiang, "Research for electromagnetic interference of automotive motor," in *2022 Asia-Pacific International Symposium on Electromagnetic Compatibility (APEMC)*, 45–48, Beijing, China, 2022.

[6] Huo, S., Z. Xue, Y. Zhou, J. Yao, and J. Bai, "Credibility assessment of EMC uncertainty analysis based on failure rate," *Progress In Electromagnetics Research Letters*, Vol. 124, 55–61, 2025.

[7] Ahmed, E. M. and K. H. Ibrahim, "GA based optimization technique for magnetic field attenuation around high voltage overhead transmission lines using mechanical rearrangement of power conductors," *Progress In Electromagnetics Research C*, Vol. 140, 185–192, 2024.

[8] Król, K. and W. Machczyński, "Optimization of electric and magnetic field intensities in proximity of power lines using genetic and particle swarm algorithms," *Archives of Electrical Engineering*, Vol. 67, No. 4, 829–843, 2018.

[9] Alameri, B. M., "Electromagnetic interference (EMI) produced by high voltage transmission lines," *EUREKA: Physics and Engineering*, Vol. 5, 43–50, 2020.

[10] Prasad, S. and T. Sidhu, "Estimation of three-phase currents in overhead power line conductors using numerical model of magnetic fields," *Progress In Electromagnetics Research C*, Vol. 97, 123–137, 2019.

[11] Lu, N., F. Zhu, Y. Xiao, Y. Chen, X. Yang, and Q. Jiang, "Electromagnetic radiation measurement and analysis of high voltage wires," in *2020 IEEE International Symposium on Electromagnetic Compatibility & Signal/Power Integrity (EMCSI)*, 650–653, Reno, NV, USA, 2020.

[12] Maniruzzaman, M., S. Ahmed, G. M. Fattah, and R. N. Toma, "Estimation of crosstalk noise for RLC interconnects in deep submicron VLSI circuit," in *2015 International Conference on Electrical Engineering and Information Communication Technology (ICEEICT)*, 1–4, Savar, Bangladesh, 2015.

[13] Hu, S., M. Tahir, J. Niu, N. Fujishima, Y. Lei, and X. He, "Analysis of mutual inductance between parallel branches for ANPC laminated busbar," in *2023 IEEE 14th International Symposium on Power Electronics for Distributed Generation Systems (PEDG)*, 1083–1087, Shanghai, China, 2023.

[14] Guo, M., S. Qin, Q. Hao, and L. Ding, "Small-signal stability modeling of AC/DC cables based on RLC circuits considering frequency dependent and mutual inductance characteristics," *IEEE Transactions on Power Delivery*, Vol. 41, No. 3, 1388–1401, Jun. 2026.

[15] Zahedi, F., E. Mehrshahi, and A. Jabbari, "On the modeling and analysis of crosstalk noise in non-identical lossy interconnects," *IEEE Transactions on Signal and Power Integrity*, Vol. 4, 197–205, 2025.

[16] Ren, K., "A hybrid quantum transport simulator for MOSFETs using non-equilibrium Green's Function and FDTD," *Progress In Electromagnetics Research M*, Vol. 137, 1–12, 2026.

[17] Chen, Y., Y. Zhang, J. Huang, J. Xu, C. Luo, and G. Guo, "Compact modeling of quantum transport in 55-nm MOSFETs at cryogenic temperatures," *IEEE Electron Device Letters*, Vol. 44, No. 9, 1392–1395, 2023.

[18] Zhao, W., M. Cheng, R. Cao, and J. Ji, "Experimental comparison of remedial single-channel operations for redundant flux-switching permanent-magnet motor drive," *Progress In Electromagnetics Research*, Vol. 123, 189–204, 2012.

[19] Yang, Y., C. Xiong, X. Chen, and H. Liu, "Electromagnetic conduction interference analysis and soft switch suppression research of electric vehicle," in *2024 8th International Conference on Electrical, Mechanical and Computer Engineering (ICEMCE)*, 579–583, Xi'an, China, 2024.

[20] Touati, S., R. Ibtiouen, O. Touhami, and A. Djerdir, "Experimental investigation and optimization of permanent magnet motor based on coupling boundary element method with permeances network," *Progress In Electromagnetics Research*, Vol. 111, 71–90, 2011.

[21] Jian, L., G. Xu, J. Song, H. Xue, D. Zhao, and J. Liang, "Optimum design for improving modulating-effect of coaxial magnetic gear using response surface methodology and genetic algorithm," *Progress In Electromagnetics Research*, Vol. 116, 297–312, 2011.

[22] Del Pino-Lopez, J. C. and P. Cruz-Romero, "Magnetic field shielding of underground cable duct banks," *Progress In Electromagnetics Research*, Vol. 138, 1–19, 2013.

[23] Costa, E. M. M., "Resonance on transformers excited by square waves and explanation of the high voltage on Tesla transformer," *Progress In Electromagnetics Research B*, Vol. 18, 205–224, 2009.